This is a preprint of a published paper, in "Computational Materials Science" by Elsevier availabe at https://doi.org/10.1016/j.commatsci.2018.11.025

Micromechanical modeling of the effect of phase distribution topology on the plastic behavior of dual-phase steels

Yuliang Hou[a,b,*], Shouyu Cai[a,*], Thaneshan Sapanathan[b,c], Alexandre Dumon[d], Mohamed Rachik[b]

[a]*School of Mechanical Engineering, Zhengzhou University, Science Road 100, 450001, Zhengzhou, China*
[b]*Laboratoire Roberval, CNRS UMR7337, Sorbonne université, Université de Technologie de Compiègne, Centre de recherche Royallieu, CS60319, 60203, Compiègne Cedex, France*
[c]*Institute of Mechanics, Materials and Civil Engineering, UCLouvain, 1348 Louvain-la-Neuve, Belgium*
[d]*ESI Group, 99 Rue des Solets, BP80112, 94513, Rungis Cedex, France*

Abstract

In this paper, a topology optimization based numerical method is proposed to investigate the micromechanical plastic behavior of dual-phase (DP) steels. Representative volume elements (RVEs) are constructed using the topology optimization based artificial microstructures. Micromechanical behavior under various loading conditions are predicted for the RVEs to investigate the plasticity, strain localization and strengthening mechanism affected by the microstructural characteristics of DP steels. Plastic strain patterns including shear band are found during the deformation. Due to the twisting movement of martensite grains, the direction of the strain localization bands in the shear loading case is 0° or 90° to the loading direction, while it is 45° in the tensile and compressive cases. Moreover, the effective flow behavior of the material under shear loading is lower than those found in tensile and compressive cases. The influence of various microstructural features, such as, martensite fraction, distribution of each phase, on the effective flow properties and the local strain partitioning has also been identified. Both of the effective flow properties and strain localization exhibit the tendency to be strengthened with the increase of martensite phase fraction. Furthermore, the RVE with more uniform martensite distribution leads to the decrease of effective flow properties and strain localization. Longer martensite-ferrite interface results from the clustering of martensite, which increases the strain localization effect during the plastic deformation.

Keywords: Dual-phase steel, Plasticity, Representative volume element, Artificial microstructure, Topology optimization

1. Introduction

Dual-phase (DP) steel contains hard martensite islands embedded into a soft ferrite matrix. Due to this specific inhomogeneous microstructure, DP steel possesses excellent mechanical properties, e.g. relatively high ultimate tensile strength (UTS), low yield to tensile strength ratio and

*Corresponding author.
Email addresses: yulianghou@zzu.edu.cn (Yuliang Hou), caishouyu@zzu.edu.cn (Shouyu Cai)

good balance between strength and formability [1–6]. Hence, DP steel becomes a promising candidate material to manufacture the car bodies in automotive industry.

Especially, the formability issues of DP steel depend on the processing methods, which are controlled either by plastic strain localization or by fracture. Moreover, the mechanical properties of martensite and ferrite phases, and the microstructural features, e.g., grain size, martensite fraction, distribution and morphology of the dispersed martensite islands [7–9] determine the plasticity and fracture behaviors of DP steel. To predict the plasticity and fracture behaviors of DP steels, numerical models of representative volume element (RVE) have been established based on their real microstructures [10–14]. Sun et al. [11] investigated driving mechanisms of fracture for different grades of DP steel using microstructure based modeling approach and found that the fracture is affected by material softening and plastic strain localization. Uthaisangsuk et al. [12, 13] successfully applied the Gurson-Tvergaard-Needleman (GTN) fracture model using an extended finite element method (XFEM) to predict the ductile failure and micro-cracks nucleation and propagation using real microstructure based RVEs during sheet metal forming of DP steels. Afterwards, stretch-forming tests under different stress states were performed on 2D RVE models to predict the fracture behavior of DP steels [14]. It was reported that, the vicinity of the interface between ferrite and martensite phases are the most critical sites for the appearance of strain localization and ductile fracture.

Besides, highly heterogeneous microstructures are obtained during welding, forging or heat treatment processes with DP steels. They exhibit specific localized microstructures; i.e., microstructure at one material point is different from another. Thus, it requires a large quantity of experimental measurements to build RVEs based on the real microstructures. However, it is relatively easier to use an artificial microstructure generated based on local phase fraction and chemical compositions to predict the flow behavior at various material points. The corresponding local phase fractions and chemical compositions can be computed from the phase transformation model incorporating appropriate diffusion mechanisms. Therefore, this approach particularly requires the development of an artificial dual-phase microstructure with similar statistical properties to replace the real one [15–22].

In recent years, geometry primitives (e.g., spheres, polygons or polyhedra) were used to generate the artificial microstructure of DP steel based on statistical descriptions. Nygårds et al. [15, 16] proposed 2D and 3D artificial microstructures of DP steels based on periodic Voronoï tessellation, with limited number of grains to predict the effective properties via simulation of uniaxial tension. Since the existing methods contain a lack of reasonable phase assignment procedure, the distribution of martensite phase was determined in a random grain growth manner. This resulted in an imprecise computation of the effective properties of DP steels. Especially, close to the yield point, the plastic behavior was not properly captured in comparison with the experimental results. In the work of Abid et al. [18], an optimization and filtering algorithm were introduced to construct tailored RVEs using Voronoï tessellation. By prescribing a Dirichlet condition (displacement-controlled tensile condition), the effect of ferrite and martensite grain size on the overall plastic behavior of DP steel was investigated. The used Voronoï tessellation was generated with pseudo-randomly distributed seeds, which underestimates the variability of the grain size, while overestimates the number of neighboring gains [18]. Furthermore, since no periodicity exists in that RVE, it is not able to generate RVE models with less than 100 µm side length.

Recently, de Geus et al. [20, 21] have investigated the plasticity and damage behaviors of DP steels using 2D and 3D microstructures. By comparing the macroscopic and microscopic mechanical responses of these two cases [20], they found that the macroscopic response of 2D models is varied more significantly than the 3D models, with the increasing volume fraction of martensite. The results of 3D models microscopically exhibited less extreme strain partitioning between different phases, compared with 2D models. Due to the constraint of the sub-surface microstructure, the hard phase in 3D models deformed more while the soft phase deformed less. Therefore, a harder macroscopic response was observed in the 3D models. Therefore, the simulation using 3D models is relatively closer to the exact solution, while 2D models are faster and provide sufficiently accurate predictions in micromechanical modeling.

Despite the above mentioned works, periodic Voronoï tessellation and an automatic phase coloring algorithm were developed by Fillafer et al. [17] to generate 3D microstructures with reliable phase assignment. Plastic strain partitioning and micro-damage initiation of DP steels were investigated using artificial microstructures generated with different martensite phase fractions. This work also considered the martensite contiguity and a "soft" optimization criteria to construct the DP microstructures with predefined controlling parameters. The influence of martensite phase fraction, grain size and dislocation density at phase interface on strain distribution and damage initiation were studied using the investigated artificial microstructures. However, the randomness of the generating seeds of Voronoï tessellation was neglected and no more detail of the "soft" criteria was given. Additionally, micromechanical modeling of DP steel under the loading conditions other than uniaxial tensile case were not considered.

In the present study, a dislocation density based approach [23] is applied to compute the flow behaviors of ferrite and martensite phases. Then, numerical tests are performed with 2D RVEs constructed using artificial microstructures, under various loading conditions (i.e., uniaxial tension, compression and shear loading). Meanwhile, the influence of various microstructural features on the effective plastic behavior is studied using a topology optimization based artificial microstructure generator. The equivalent stress-strain distributions that result from different loading conditions provide better understanding of local deformation process at microscopic level.

2. Artificial microstructure generation

A topology optimization based artificial microstructure generator was proposed in our previous study [4]. Using this novel method, artificial RVEs were developed with an *enhanced phase assignment algorithm* combined with a *modified Voronoï tessellation*. The *modified Voronoï tessellation* was periodically generated from Halton (quasi-random) sequence [24] which statistically exhibits lower discrepancy and thus it provides adequate grain morphology. For this method, two controlling parameters were obtained from the statistical microstructure description of DP steels [17]. By defining objective and constraint functions of these two controlling parameters, the proposed phase assignment algorithm based on the density-based methods in topology optimization [25–27], was applied to achieve an appropriate phase distribution. The artificial DP microstructure generation is governed by a mathematical approach. Although this approach does not have the capability to describe the real physicochemical procedure of martensite nucleation and growth, it enables to appropriately represent the microstructures of heterogeneous materials

(materials may consist of two or more phases). The generated microstructure is suitable for flow stress homogenization. Then, the effective plastic behavior was computed using an asymptotic expansion homogenization (AEH) scheme [28]. This section will focus on the brief overview of the artificial microstructure generator.

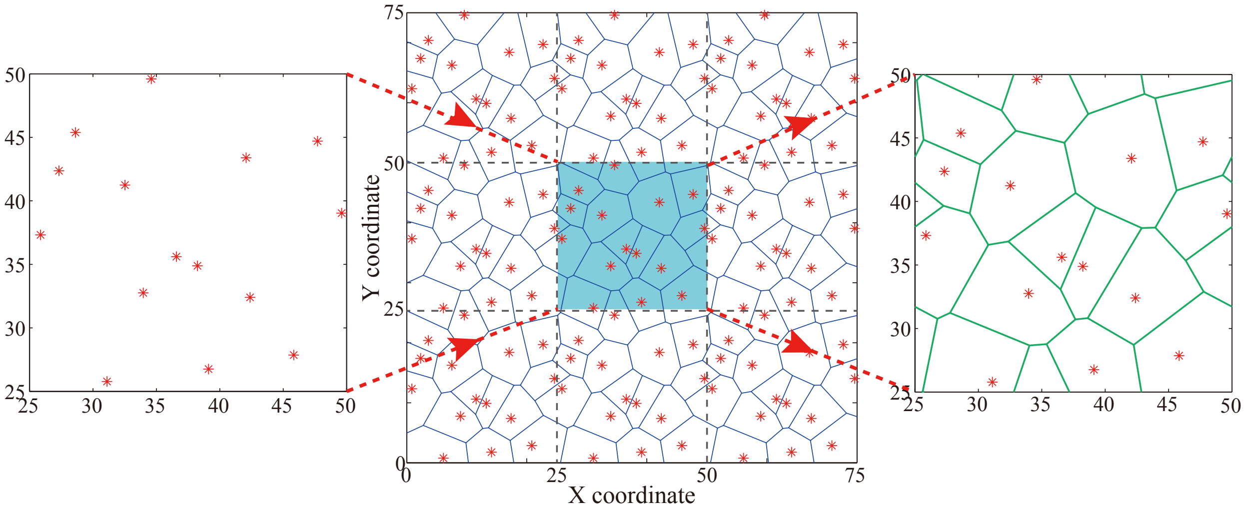

(a) (b) (c)

Figure 1: Construction process of the *modified Voronoï tessellation*: (a) seeds selected from Halton sequence; (b) tessellation generated using Voronoï algorithm and a periodic set of seeds; (c) the final *modified Voronoï tessellation*.

Throughout the application of Halton sequence, the distribution of the sampling points that are considered as the Voronoï seeds, is more uniform than that of pseudo-random sequence. The *modified Voronoï tessellation* constructed using Halton sequence, effectively avoids the appearance of grains with extreme size and bad aspect ratio within the tessellation. Moreover, due to the favorable numerical properties in the context of computational homogenization, these seeds are repeated three times in each direction to ensure the periodicity of the obtained Voronoï tessellation. With these periodically distributed seeds selected from Halton sequence, a square periodic tessellation is constructed using Voronoï algorithm. Fig. 1 illustrates the construction process of the *modified Voronoï tessellation*. A set of 15 generating seeds, whose abscissas and ordinates are selected from Halton sequence, is located in the domain of $\{(x, y) \in [25, 50]\}$ (Fig. 1a). By performing the periodicity treatment for these seeds, a Voronoï tessellation (with the total of 135 polygons) is generated (Fig. 1b). Then, the center region in the obtained tessellation (the square with blue background color in Fig. 1b) is extracted as the *modified Voronoï tessellation*, as shown in Fig. 1c.

In addition to the *modified Voronoï tessellation*, an automated process is used to assign the selected cells to represent different phases. Within this automated process, the *modified Voronoï tessellation* is considered as a fixed grid (Fig. 2a), as similar to the method in material topology optimization. In each modified Voronoï cell, a material density function is proposed to determine its phase property: martensite cells with density $\rho = 1$, (red layer in Fig. 2b), while ferrite cells with density $\rho = 0$ (blue layer in Fig. 2b). By defining constraints and an objective function, this process is deduced to a 0-1 discrete value optimization problem, also known as “black-and-white” design [25]. Therefore, the material interpolation algorithms in topology optimization is referred to achieve an artificial microstructure with proper phase distribution, as shown in Fig. 2c.

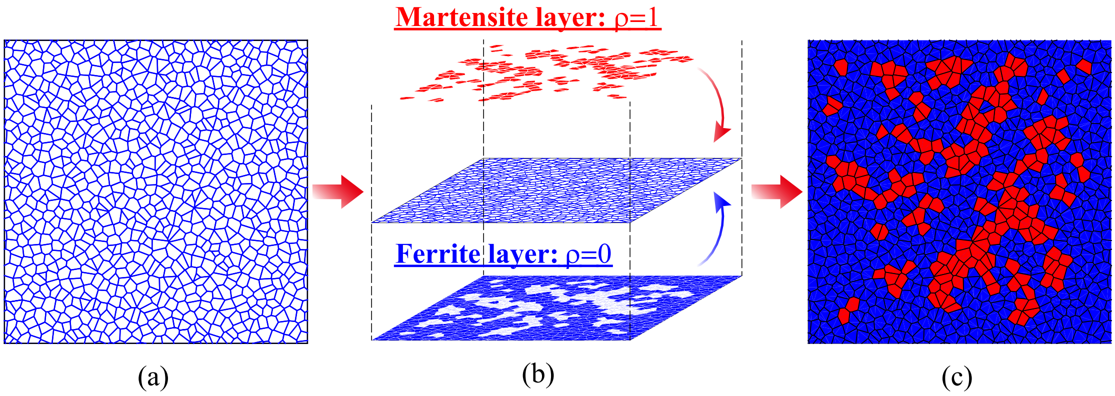

Figure 2: Enhanced phase assignment process: (a) *modified Voronoï tessellation*, (b) phase assignment and (c) final DP microstructure.

In order to perform the phase assignment procedure, two design parameters proposed by Fillafer et al. [17], are implemented in this study to confine the solution space. These two parameters are the martensite phase fraction (P_M) and the neighboring coefficient of martensite grains (C_M). Thus, this method considers both the martensite phase fraction and the correlation between different martensite islands. The expressions of these two parameters are given by:

$$P_M = \frac{A_M}{A_T}, \quad C_M = \frac{2L_{MM}}{2L_{MM} + L_{FM}} \tag{1}$$

where, A_M and A_T denote martensite phase and total areas; L_{MM} and L_{FM} are length of specific martensite-martensite and martensite-ferrite grain boundaries, respectively. It is also identified that the value of P_M can vary between 0 and 1, but for a given martensite phase fraction, C_M cannot satisfy the range between 0 and 1. In other words, these two design parameters are not mutually independent.

According to the algorithm related to density-based topology optimization method, the design parameters are rewritten in a matrix form, in which a distributed and discrete value problem is formulated. To solve this problem, the most commonly used approach in topology optimization is to replace the integer by continuous variables. And then, a penalty factor is introduced to derive the martensite density distribution as same as the so-called “black-and-white” solution [25]. Therefore, a structural optimization problem is obtained by defining the target input parameters P_M^{target} and C_M^{target}, which are identified based on the statistical descriptions of a given DP steel. A heuristic updating scheme [25] is then introduced to solve the optimization problem.

Following the aforementioned process, artificial DP microstructures are constructed with good convergence. That is, if the design parameters and the Voronoï tessellation are fixed, the generator will find only one unique optimal solution. Using the *modified Voronoï tessellation* and the predefined sets of design parameters, two example artificial microstructures are constructed as shown in Fig. 2c. In this artificial microstructure, the target design parameters are set as, $P_M^{target} = 0.22$ and

$C_M^{target} = 0.30$. A fast and stable convergence is achieved with 9 iterations, the resulted microstructure has $P_M = 0.22$ and $C_M = 0.29$. As discussed previously, due to the mutual independence of these two parameters (P_M and C_M), there exists a slight dissimilarity between the target and result parameters. Furthermore, a proper orthogonal decomposition (POD) approach [4] has been developed to identify the optimal controlling parameters. Some other recent works [29, 30] also considered the POD approach to identify mechanical parameters for metallic materials using nano-indentation. The POD approach provides the additional advantage of the relatively high efficiency, thus it has also been applied in this study.

3. Numerical implementation

3.1. Flow behaviors of ferrite and martensite phases

In the work of Jafari et al. [31], the stress-strain behavior of ferrite phase has been predicted using a dislocation based theory [23] and a crystal plasticity model [32], respectively. Their comparison between these two approaches clearly indicates that there is no obvious difference between predicted results using both methods [31]. Therefore, to perform the finite element (FE) analysis of the DP steel, the stress-strain relation of each constituent phase is computed using the dislocation based theory, in which material parameters are calculated using the local chemical composition. It was reported that the flow behavior of martensite phase is mainly affected by the carbon content and the back stress [33]. Nevertheless, the formulation of flow behavior using the dislocation based theory without taking into account for the back stress, has been widely used in the studies [34, 35]. The same dislocation based theory is considered in this study to describe the flow behaviors of the ferrite and martensite phases. Moreover, the FE model does not consider the crystal plasticity behavior and the effect of different crystal orientations in the stress-strain calculation. Concerning the dislocation based method, the stress-strain relation is expressed as [34, 35]:

$$\sigma = \sigma_0 + \Delta\sigma + \alpha M \mu \sqrt{b} \sqrt{\frac{1 - \exp(-M k_r \varepsilon_p)}{k_r L}} \quad (2)$$

where α is a constant ($\alpha = 0.33$), M is Taylor factor ($M = 3$), μ is the shear modulus ($\mu = 80$ GPa), b is Burger's vector, L is the average dislocation free path, and k_r is the dislocation recovery rate.

Table 1: Chemical composition of the DP980 steel (in wt%).

C	Si	Mn	Ni	P	Cu	Cr	Mo
0.09	0.31	1.67	0.01	0.008	0.01	0.21	0.01

The first term σ_0 in Eq. (2) is the Peierls stress caused by dislocation movement. It can be calculated using:

$$\sigma_0 = 77 + 750\%\mathrm{P} + 60\%\mathrm{Si} + 80\%\mathrm{Cu} + 45\%\mathrm{Ni} + 60\%\mathrm{Cr} + 80\%\mathrm{Mn} + 11\%\mathrm{Mo} + 5000 N_{SS} \quad (3)$$

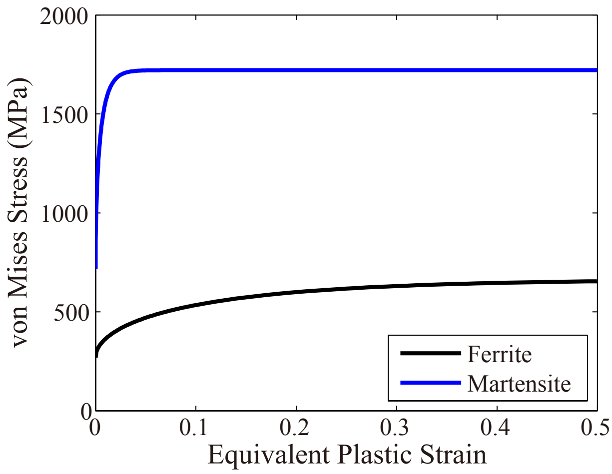

Figure 3: Flow behaviors of ferrite and martensite phases obtained from the DP980 steel.

where, N_{SS} denotes the carbon content (in wt.%) in DP steel. The second term $\Delta\sigma$ in Eq. (2) is the additional strengthening due to the precipitation and carbon in solid solution. For the ferrite phase, it can be calculated as:

$$\Delta\sigma = 5000 C_{SS}^{F} \tag{4}$$

For the martensite phase:

$$\Delta\sigma = 3065 C_{SS}^{M} - 161 \tag{5}$$

where, C_{SS}^{F} and C_{SS}^{M} denote the carbon content (in wt.%) in ferrite and martensite, respectively.

Table 2: Material constants of the DP980 steel.

Phase	L(m)	k_r	C_{SS} (wt%)
Ferrite	5.0×10^{-6}	2	0.004
Martensite	3.8×10^{-8}	41	0.206

The reference material parameters used in this study are obtained from a DP980 steel. Chemical composition and material constants of constituent phases obtained from energy dispersive X-ray (EDX) spectroscopy analysis, which are listed in Tables 1 and 2, respectively. The obtained flow behavior of each phase is depicted in Fig. 3. The martensite phase exhibits a limited hardening behavior because of the absence of the back stress in the description of the flow behavior. The elastoplastic stress-strain relation with isotropic hardening is considered for both ferrite and martensite phases.

3.2. Micromechanical modeling

According to de Geus et al. [19, 20], the dissimilarities of simulation results between 2D and 3D microstructures were not significant. Moreover, when the 2D microstructures are extended into 3D ones, the computational time significantly increases during the microstructure generation and FE calculation. Therefore, 2D microstructures are used in this study. The FE models of the 2D artificial RVEs, generated using the combination of the *modified Voronoï tessellation* and enhanced phase assignment algorithm, are constructed within ABAQUS/Standard software [36]. The effect of RVE and mesh sizes has already been investigated in a recent study by Ramazani et al. [35]. The acceptable size of RVE for a DP steel is considered with minimum of 24 μm edge length and it contains at least 19 martensite islands. By prescribing periodic boundary condition, this RVE size is sufficiently large to represent all microstructural features while it also remains small enough to be considered as statistically homogeneous during the computation of effective flow properties. Likewise, we include 2D RVE models with the size of 25 μm × 25 μm.

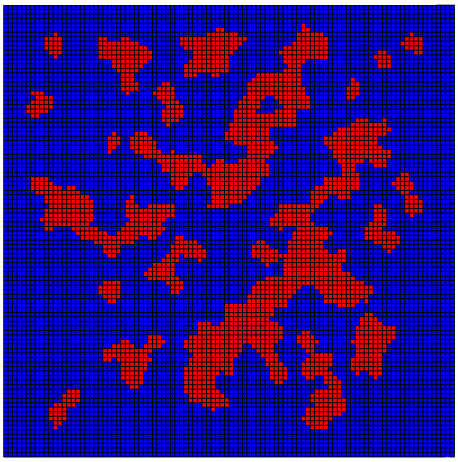

Figure 4: Meshed FE model with 0.25 μm element size and 25 μm edge length of the artificial RVE example shown in Fig. 2a.

In addition, element length between 0.1 and 2 μm was further used to discretize the 2D RVE model. No deviation in the results is found for elements finer that 0.25 μm. Numerical simulation of 2D microstructure with planar assumption was compared with the actual 3D one [20], it indicated that the dimensionality effect on macroscopic and microscopic response was quite limited. Therefore, linear elements with 0.25 μm size and plane strain assumption are applied to the micromechanical model. Fig. 4 shows the meshed FE model (with the mesh size of 0.25 μm) of the artificial RVE example given in Fig. 2c. Using this mesh size, strain partition along the martensite-ferrite interface is effectively captured, which reach a good agreement with former studies [18, 35].

3.3. Periodic boundary conditions of various loading scenarios

Appropriate boundary conditions can guarantee both displacement and traction continuity on the two opposite sides of the micromechanical model which are essential to achieve accurate results. Compared with conventional Dirichlet (displacement) and Neumann (constant traction) conditions, periodic boundary condition provides more accurate prediction of the effective mechanical properties [37]. Therefore, periodic boundary condition is chosen for the micromechanical modeling of various loading scenarios, which include uniaxial tension, compression and shear loading conditions.

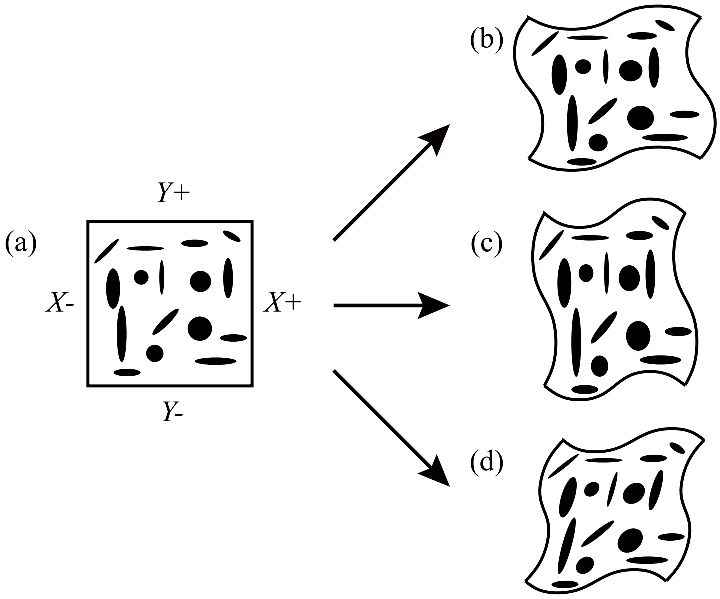

Figure 5: Schematic illustration of (a) original and deformed RVE models with the periodic boundary conditions of (b) tension in x direction, (c) tension in y direction, and (d) shear.

Concerning periodic boundary condition, the displacement field of the periodic RVE is prescribed as in the following equation [37]:

$$u_i = \bar{\varepsilon}_{ij}\phi_j + u_i^* \tag{6}$$

where, $\bar{\varepsilon}_{ij}$ is the macroscopic average strain of the RVE model, ϕ_j is the node coordinate of the RVE model, and u^* is a periodic function which comes from one RVE to another nearby. Hence, respective displacement for the two opposite boundaries is given by:

$$u_i^{k+} = \bar{\varepsilon}_{ij}\phi_j^{k+} + u_i^* \tag{7}$$

$$u_i^{k-} = \bar{\varepsilon}_{ij}\phi_j^{k-} + u_i^* \tag{8}$$

where, $k = x, y$ in 2D case, and $k+, k-$ represent the opposite boundaries perpendicular to the k-direction.

Combining Eqs. (7) and (8), the difference in displacement between these two opposite boundaries of RVE models is obtained as:

$$u_i^{k+} - u_i^{k-} = \bar{\varepsilon}_{ij}\Delta\phi_j^k \tag{9}$$

where, $\Delta\phi_j^k$ is a constant for any parallelepiped RVE model. The schematic illustration of periodic boundary conditions under different loading scenarios is illustrated in Fig. 5. Fig. 5a shows the original RVE model with two pairs of parallel boundaries, $(X-, X+)$ and $(Y-, Y+)$. After that, different loading conditions are defined using the displacement constraints. The displacement constraints are prescribed on these two pairs of RVE boundaries, and they are computed according to Eq. (9). The detailed formulation for each loading condition is given by:

$$\text{Tension in x direction:} \quad u_x^{X+} - u_x^{X-} = \bar{\varepsilon}_{xx}\Delta\phi_x^X \tag{10}$$

$$\text{Tension in y direction:} \quad u_y^{Y+} - u_y^{Y-} = \bar{\varepsilon}_{yy}\Delta\phi_y^Y \tag{11}$$

$$\text{Shear:} \quad u_x^{Y+} - u_x^{Y-} = \bar{\varepsilon}_{xy}\Delta\phi_x^Y, \quad u_y^{X+} - u_y^{X-} = \bar{\varepsilon}_{xy}\Delta\phi_y^X \tag{12}$$

Fig. 5b, c and d show the deformed RVE models with periodic boundary conditions of tension in x and y directions and shear loading cases. Additionally, the periodic boundary condition of compression in each direction can also be expressed using Eqs. (10) and (11), in which the corresponding average strain components are negative. In Section 4.1, numerical tests are performed with different periodic boundary conditions.

3.4. Homogenization scheme

Asymptotic expansion homogenization (AEH) [28] is employed to compute the effective flow properties of DP steels based on the RVE modeling. Therefore, the effective stress and strain components at the macroscopic level are calculated using the volume average of the microscopic components using the following equations:

$$\bar{\sigma}_{ij} = \frac{1}{V_{RVE}} \int_{V_{RVE}} \sigma_{ij} dV \tag{13}$$

$$\bar{\varepsilon}_{ij} = \frac{1}{V_{RVE}} \int_{V_{RVE}} \varepsilon_{ij} dV \tag{14}$$

where, $\bar{\sigma}_{ij}$ and $\bar{\varepsilon}_{ij}$ are the macroscopic homogenized components of stress and strain , σ_{ij} and ε_{ij} are the stress and strain components obtained from RVE modeling.

4. Results and discussion

The investigated artificial RVE is generated according to the statistical description of microstructural features of DP980 steel. Using the POD approach [4], the target controlling parameters for this DP steel are identified as $P_M = 0.55$ and $C_M = 0.50$. The RVE and corresponding FE model are shown in Fig. 6a and b, respectively. Further investigations are performed based on the obtained micromechanical model combined with the flow behaviors of constituent phases.

4.1. Numerical tests under different loading conditions

4.1.1. Uniaxial tension test

A uniaxial tension test with the loading in x direction, which prescribes a macroscopic deformation of 10% in x-direction, is performed using the FE model given in Fig. 6b. Therefore, according to Eq. (10), constraints are utilized to impose the corresponding periodic boundary conditions for the micromechanical model.

Fig. 7a and b show the von Mises stress and equivalent plastic strain distributions at the macroscopic plastic strain level of 8.08%, respectively. Significantly high local stresses are noticed within the martensite islands, while relatively low local stresses appear within the ferrite matrix.

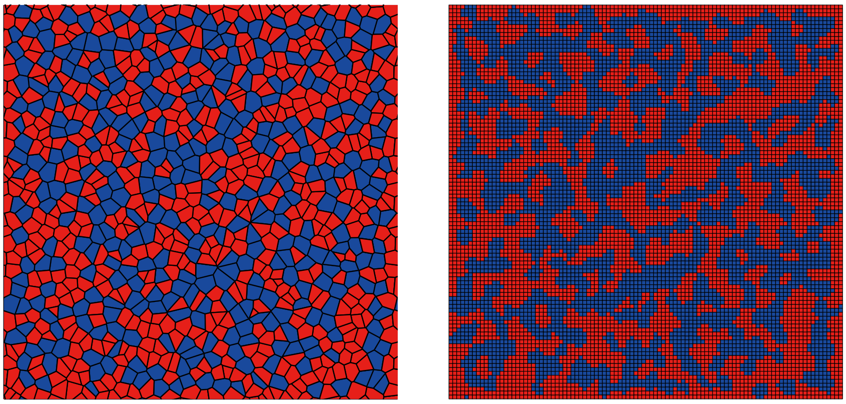

(a) (b)

Figure 6: (a) RVE and (b) FE models generated with the target controlling parameters: $P_M^{target} = 0.55$ and $C_M^{target} = 0.50$ for DP980 steel. (Red and blue cells represent martensite and ferrite grains, respectively.)

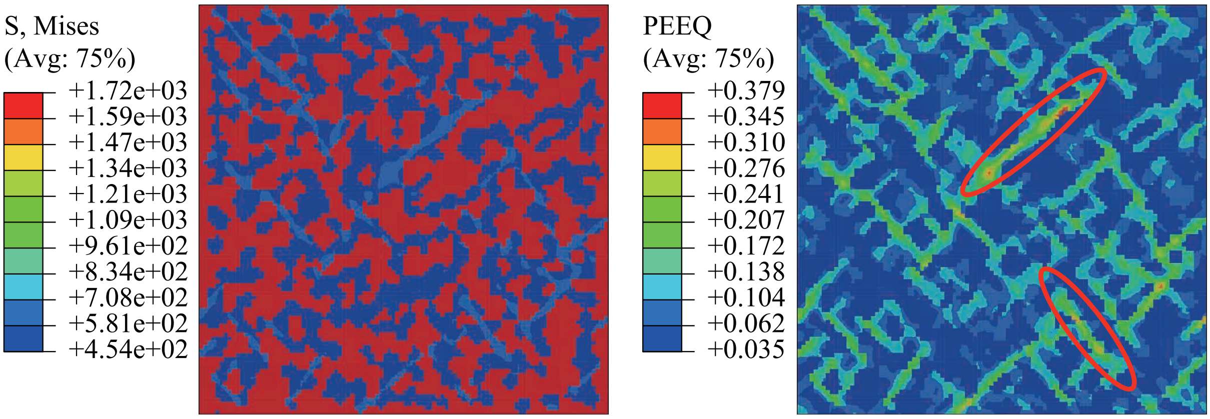

(a) (b)

Figure 7: Distribution of: (a) von Mises stress (MPa) and (b) equivalent plastic strain obtained for the artificial RVE at the macroscopic plastic strain level of 8.08% for the uniaxial tension test. (Shear bands are in red ellipses.)

Moreover, the average stress in ferrite phase is much lower than that in the martensite phase. Since no material fracture or damage model is introduced, the formation of shear bands are clearly observed in the ferritic matrix along martensite islands (Fig. 7b). These shear bands and localized plastic strain distributions are caused by the specific heterogeneous microstructure of the DP steel. In the uniaxial tension case, the direction of these shear bands is around 45° to the tensile loading direction (i.e., x direction).

4.1.2. Uniaxial compression test

A uniaxial compression test is performed with the macroscopic plastic strain of -10% in x-direction for the same RVE model with the boundary condition described in Eq. (10). Corresponding distributions of von Mises stress and equivalent plastic strain at the macroscopic plastic strain level of -8.01% are shown in Fig. 8a and b, respectively. Similar to that of the tensile loading case, high stresses and shear bands are found in the martensite islands and ferrite matrix, respectively. The direction of these shear bands is also around ±45° to the compressive loading direction. Therefore, if a ductile damage model is adopted, as plastic strain localization accumulating, voids and microcracks are expected to nucleate along the martensite-ferrite interfaces.

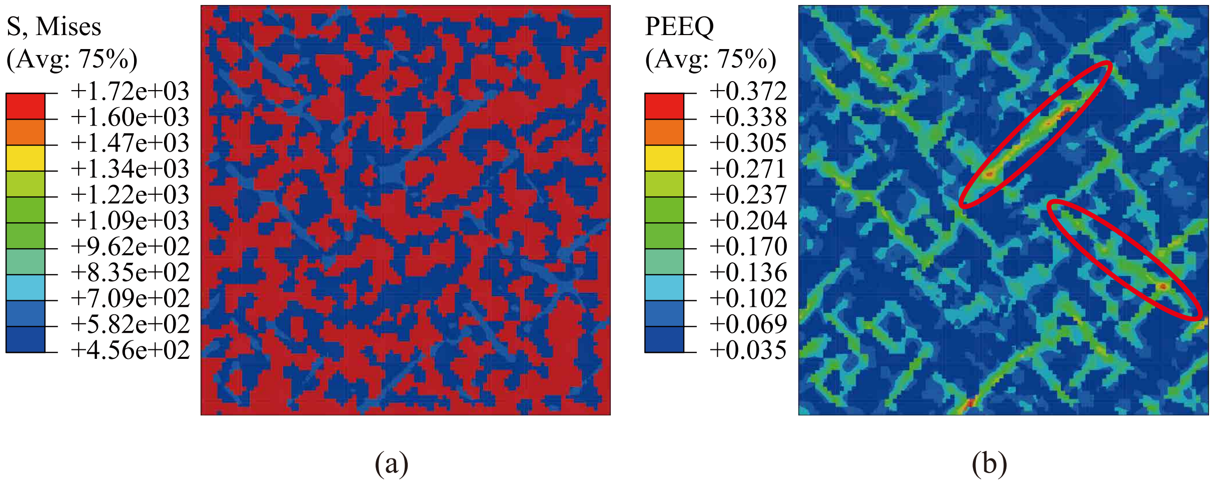

Figure 8: Distribution of: (a) von Mises stress and (b) equivalent plastic strain in artificial RVE at macroscopic plastic strain level of -8.01% for the uniaxial compression test. (Shear bands are in red ellipses.)

4.1.3. Shear test

Shear periodic boundary conditions are prescribed with the macroscopic shear deformation of 10% for the RVE model using Eq. (12). Consequently, the related distributions of von Mises stress and equivalent plastic strain at macroscopic strain level of 8.05% are obtained as shown in Fig. 9a and b, respectively.

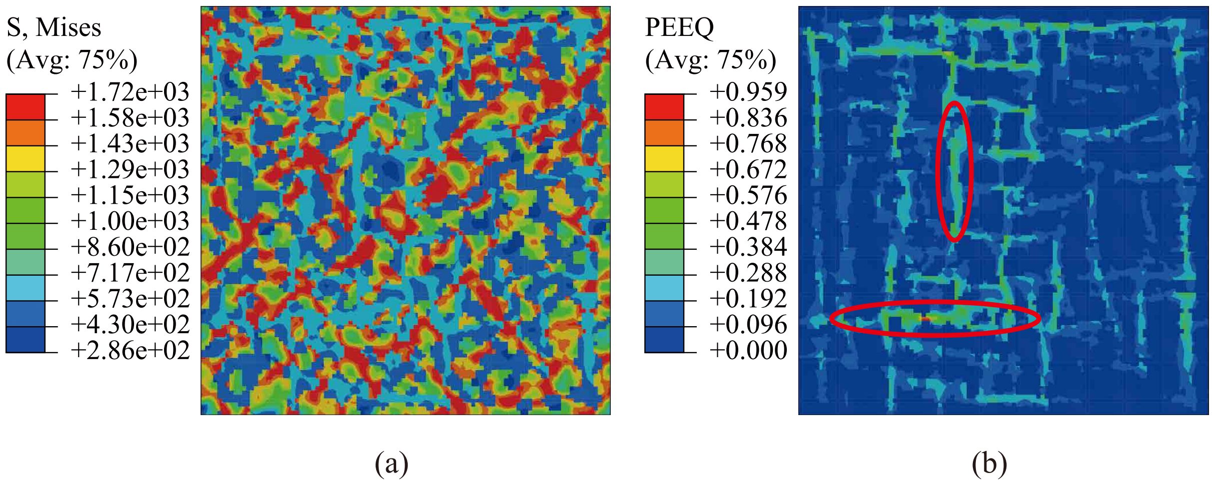

Figure 9: Distribution of: (a) von Mises stress and (b) equivalent plastic strain in the artificial RVE at the macroscopic plastic strain level of 8.05% obtained for the shear loading condition. (Shear bands are in red ellipses.)

In comparison with the uniaxial tensile and compression tests, the shear test also shows the maximum stress within the martensite islands. Similarly, the average stress in martensite phase is relatively higher than that in the ferrite phase. However, the von Mises stress distributions in martensite and ferrite phases vary more significantly for the shear test than that of other two cases (uniaxial tensile and compressive tests). Furthermore, strain localization zones are formed within the ferrite matrix near martensite grains. However, their directions are either horizontal or vertical in the local coordinate system (Fig. 9b), and they differ with those two previous cases. Moreover, the plastic strain peak that appeared in this case is 0.959, which is the highest among all three cases for approximately same macroscopic plastic strain. The main reason for the increased plastic strain during the shear loading is that, the martensite grains accommodate a relative twisting movement within the ferrite matrix due to the mismatch in the flow behaviors of individual phases [38]. Thus, the twisting movement leads to the phenomenon of the neighboring ferrite grains to be stretched to a larger value than that occurs during a uniaxial loading condition. Therefore, the strain localization zones caused by the shear periodic boundary conditions are oriented in horizontal or vertical directions. And, the accumulation of the plastic strain in the ferrite matrix forms in a more concentrated ways. Additional investigation needs to be implemented using experimental approaches to support this conclusion.

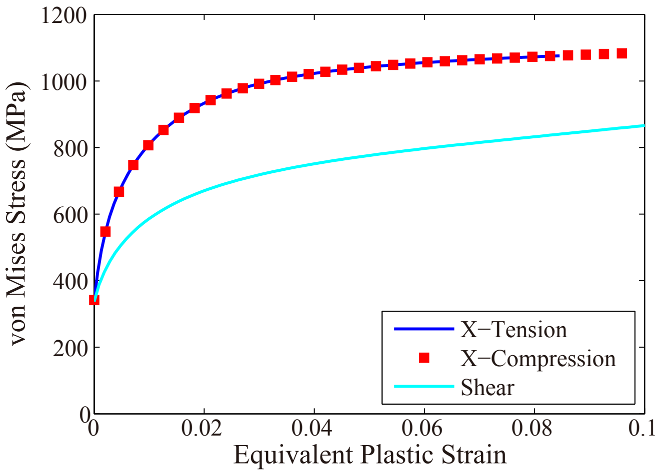

Figure 10: Homogenized plastic stress-strain behaviors of RVE model with various loading conditions.

To further investigate the effective plastic behaviors of DP steel under different loading scenarios, homogenized plastic stress-strain relations are computed using the AEH scheme. The homogenized plastic stress-strain curves of uniaxial tension, compression and shear are depicted in Fig. 10. In comparison, the curves of tension and compression tests are almost overlapped, and they differ from the curve obtained for the shear test. That is, as the plastic flow accumulating, significantly large deformation of ferrite phase is caused by the twisting movement of martensite grains during the shear test. Due to the non-existence of the twisting movement in tension and compression tests, the homogenized stress-strain responses are similar in both cases.

During the deformation of each constituent phase, a large strain localization is presented and accumulated within the ferrite phase before macroscopic fracture emerges. Generally, the macroscopic fracture initiation in the ferrite matrix shows a dependency on the stress state, while the stress triaxiality η is used as a representation of the stress state to describe the threshold of ductile fracture in metals. The stress triaxiality is defined as the ratio between the hydrostatic stress σ_m and von Mises equivalent stress σ_v:

$$\eta = \frac{\sigma_m}{\sigma_v} = \frac{\frac{1}{3}(\sigma_{\mathrm{I}} + \sigma_{\mathrm{II}} + \sigma_{\mathrm{III}})}{\sqrt{\frac{1}{2}[(\sigma_{\mathrm{I}} - \sigma_{\mathrm{II}})^2 + (\sigma_{\mathrm{II}} - \sigma_{\mathrm{III}})^2 + (\sigma_{\mathrm{I}} - \sigma_{\mathrm{III}})^2]}} \tag{15}$$

where, $\sigma_{\text{I-III}}$ are the principal stresses. The macroscopic triaxiality $\bar{\eta}$ is used to describe the stress state for a RVE model under a given loading condition that can be expressed as:

$$\bar{\eta} = \frac{\bar{\sigma}_m}{\bar{\sigma}_v} \tag{16}$$

where $\bar{\sigma}_m$ and $\bar{\sigma}_v$ denote the macroscopic hydrostatic and von Mises stresses, respectively. To compute $\bar{\sigma}_m$ and $\bar{\sigma}_v$, the macroscopic stress tensor of the RVE model is initially calculated using Eq. (13) and the stress tensor of each finite element, which is extracted from the FE computation at a given loading increment. The macroscopic triaxialities of different loading conditions are obtained using Eq. (16), and indicated in Fig. 11. Based on the theoretical calculations [39], the macroscopic triaxialities are expected to be 1/3, -1/3 and 0 for uniaxial tension, uniaxial compression and shear loading conditions, respectively. However, the homogenized macroscopic triaxialities $\bar{\eta}$ obtained from the simulation, are 0.338, -0.321 and 0.024 for these loading conditions. The difference between the computed and analytical triaxialities is not significant, and it is mainly resulting from the computation of the macroscopic stress tensor in a homogenized manner.

In the work of de Geus et al. [40, 41], it was reported that, the soft matrix dominates the macroscopic fracture initiation at low stress triaxiality, while the hard inclusion takes over with the increase of triaxiality. Moreover, different macroscopic triaxialities, especially high values of applied triaxiality, lead to different macroscopic plastic behaviors but similar shear bands around fracture initiation sites [40]. Therefore, the relation between stress triaxialities and local strain distribution should be analyzed to study the fracture initiation for all loading scenarios. Distributions of equivalent plastic strain and stress triaxiality at the same macroscopic plastic strain level of those three loading cases are also depicted in Fig. 11.

From these contours of equivalent plastic strain in Fig. 11a-c, it could be seen that, strain localization occurs non-uniformly and differently in the microstructures with regard to the applied stress states. For uniaxial tension ($\bar{\eta} = 0.338$) and compression ($\bar{\eta} = -0.321$), similar formation of shear bands (±45° to loading directions) appear in the vicinity of interfaces between martensite and ferrite phases. In these two loading scenarios, high triaxialities with positive and negative values are located in the martensite islands (Fig. 11d and e), while relatively low triaxialities appear in the ferrite matrix. Ductile fracture initiation is prone to take place within the ferrite matrix nearby the martensite-ferrite interface as plastic flow accumulating, which agrees with results concluded by de Geus et al. [40]. In the case of shear loading ($\bar{\eta} = 0.024$), shear band formation becomes prevalent mechanism, especially at the areas with sharp and narrow intersecting corners between the two phases. The triaxiality within the RVE model under shear condition is distributed more uniformly

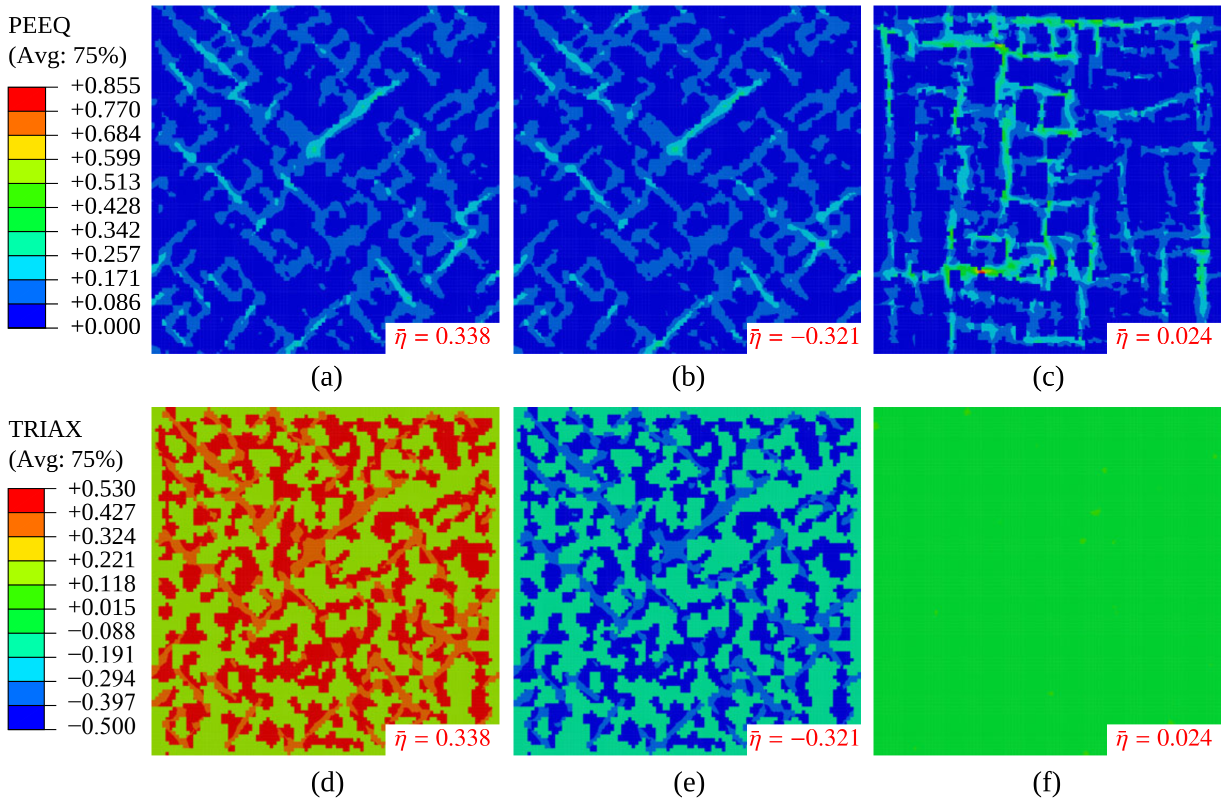

Figure 11: Distribution of equivalent plastic strain (a-c) and stress triaxiality (d-f) obtained for the artificial RVE at the macroscopic plastic strain level of 7.08% under the loading conditions of, uniaxial tension: (a) and (d), uniaxial compression: (b) and (e), and shear: (c) and (f).

than the other two cases. And, the triaxiality of both martensite and ferrite element is approximately equal to 0, whose absolute value is lower comparing with uniaxial tension and uniaxial compression loading. Meanwhile, higher equivalent plastic strain appears along the martensite-ferrite interface under shear loading condition. Hence, stress states of pure or quasi-pure shear loading condition indicates that the fracture initiation could occur at an early stage of deformation process than that of uniaxial tension and compression.

4.2. Influence of microstructural features on microscopic and macroscopic plastic behaviors

In this section, numerical tension tests with periodic boundary conditions are performed to understand the effect of martensite phase fraction and its distribution, on the microscopic and macroscopic plasticity behaviors. Simulation of the RVE models are performed until the macroscopic strain reaches 10% in x direction.

4.2.1. Effect of martensite phase fraction

Due to the difference in mechanical properties of the constituent phases in DP steels, the phase fraction of martensite affects the effective properties of DP steel [35]. Thus, the effect on the microscopic strain distribution during the deformation caused by various martensite phase fraction is investigated using the artificial RVEs.

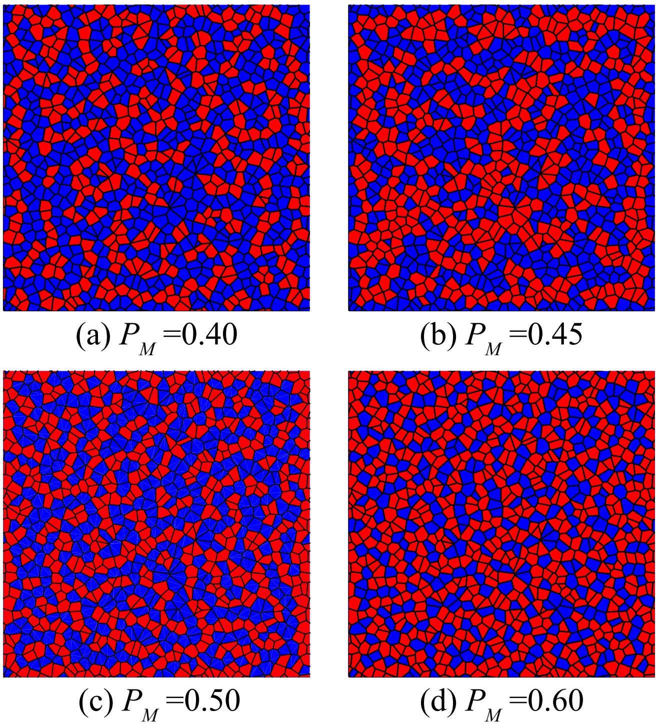

Figure 12: RVEs generated with $C_M = 0.50$, and by varying the parameter P_M as (a) $P_M = 0.40$, (b) $P_M = 0.45$, (c) $P_M = 0.55$ and (d) $P_M = 0.60$. (Red and blue cells represent martensite and ferrite grains, respectively.)

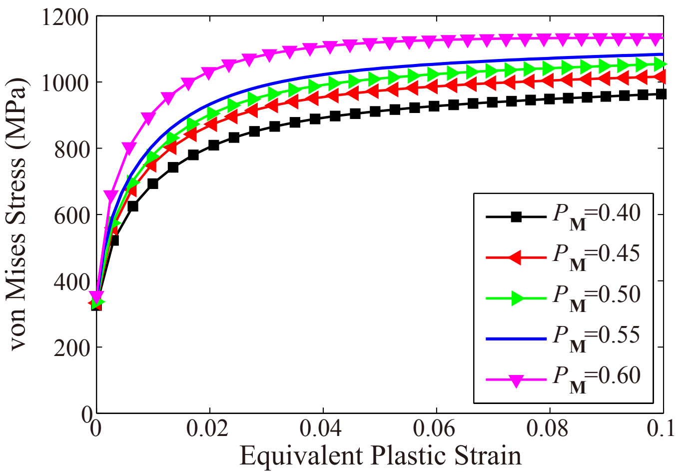

Figure 13: Homogenized plastic stress-strain relations of RVEs generated with $C_M = 0.50$ and with various values of P_M.

RVEs of 5 artificial DP microstructures with 900 grains are constructed with $C_M = 0.50$, and having P_M in the range of [0.40, 0.60], as shown in Figs. 6a and 12. By applying the periodic boundary condition of uniaxial tension for these RVE models, the effective macroscopic properties are calculated using Eqs. (13) and (14), as shown in Fig. 13. It is identified that the effective flow properties are improved with the increase of the target controlling parameter P_M, and it is also in agreement with the conclusions of another recent study [35].

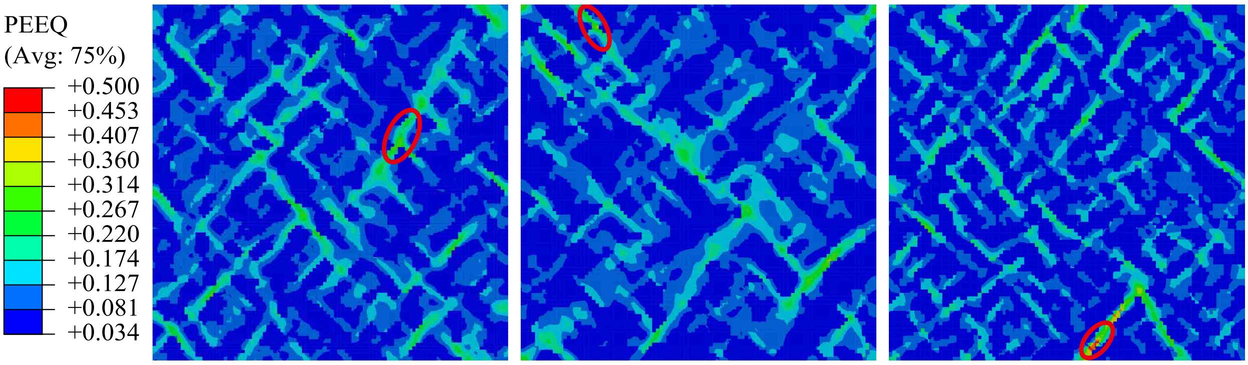

(a) (b) (c)

Figure 14: Influence of parameter P_M on the microscopic plasticity behavior: equivalent plastic strain distribution of RVEs generated with $C_M = 0.50$ and P_M equal to (a) 0.40, (b) 0.50 and (c) 0.60, at the macroscopic strain level of 8.08%. (The region with maximum values of plastic strain are located using red ellipses.)

Fig. 14 illustrates the equivalent plastic strain distributions of RVEs generated with P_M equal to 0.40, 0.50 and 0.60 at the macroscopic strain level of 8.08%. This result indicates that the appearance of shear bands mainly occurs within the ferrite matrix. However, the maximum microscopic plastic strain in these RVEs are different: in the cases of P_M equal to 0.40, 0.50 and 0.60, the maximum values are 0.306, 0.358 and 0.491, respectively. This result emphasizes that, the increase of martensite fraction leads to the increase in strain localization. Moreover, as the martensite fraction increases from 0.40 to 0.50, the plastic strain peak within the ferrite phase is increased only by 0.052. After that, when the martensite fraction comes to 0.60, this peak is increased by 0.133. It confirms that, the plastic strain peak exhibits a nonlinear evolution with the controlling parameter P_M.

4.2.2. Effect of martensite phase distribution

To investigate the influence of martensite phase distribution on the macroscopic and microscopic properties of DP steel, the parameter C_M is used to control the aggregation of martensite grains. Four artificial microstructures are generated, with $P_M = 0.55$ and with C_M equals to 0.43, 0.48, 0.50 and 0.55, as shown in Figs. 6a and 15.

Fig. 16 shows the homogenized plastic stress-strain curves of these RVEs, in which the same uniaxial tensile boundary conditions are applied. Due to the same martensite phase fraction used to generate these RVEs, small differences are noticed between the effective flow stress curves. The martensite phase distribution in the first two (Figs. 15a and b) is less clustered than in the case of the third one (Fig. 15c). From this comparison, it is evident that the RVE with smaller C_M underestimates the plastic behavior of DP steel (Fig. 16). The main reason is that, the interface length between ferrite and martensite in the RVE with smaller C_M is longer than the one with larger C_M. Since the existing heterogeneity at grain level tends to cause the strain localization, and the microstructure with longer martensite-ferrite interface boundary is likely to require less energy to perform the same amount of plastic deformation.

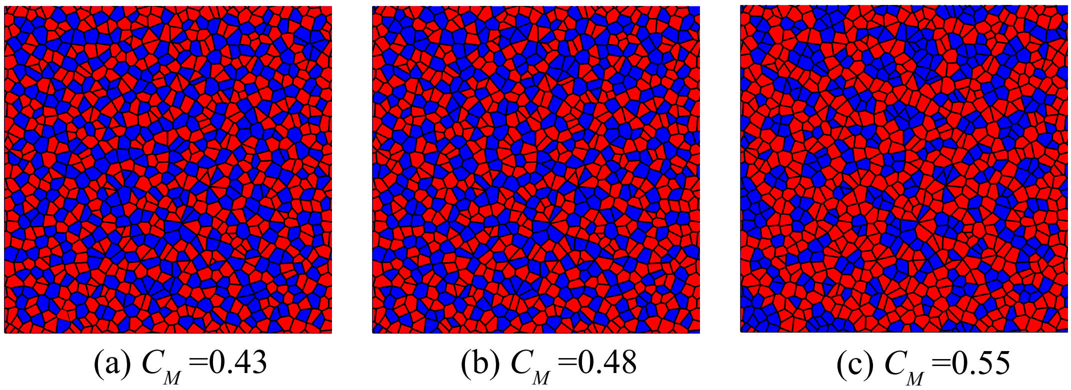

Figure 15: RVEs generated with $P_M = 0.55$ and various values of C_M. (Red and blue cells represent martensite and ferrite grains, respectively.

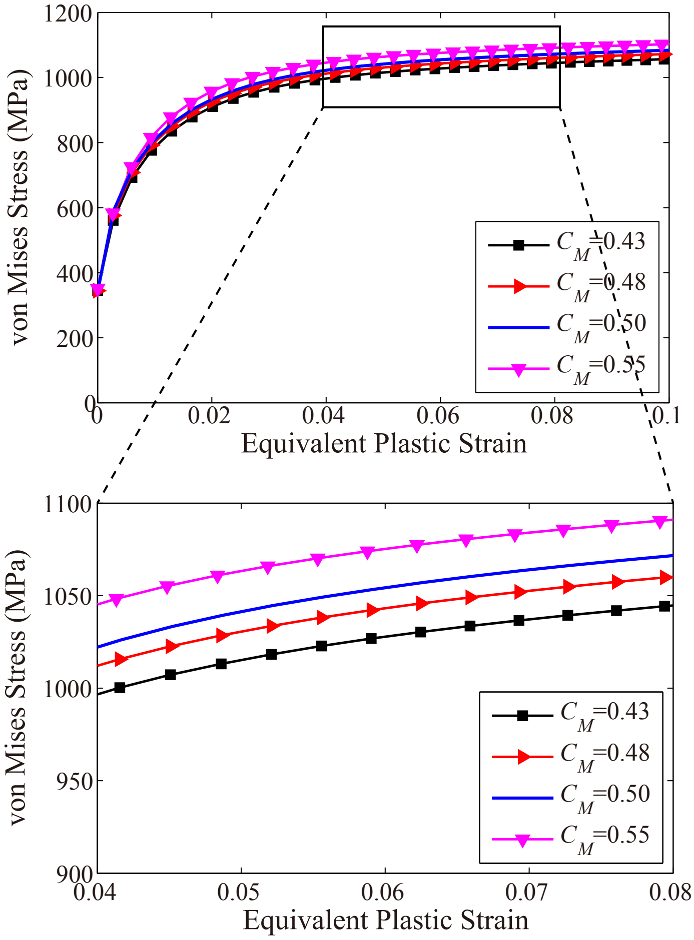

Figure 16: Homogenized plastic stress-strain relations of RVEs generated with $P_M = 0.55$ and various values of C_M.

Moreover, the influence of parameter C_M on the microscopic plasticity behavior is investigated based on the equivalent plastic strain distribution at the macroscopic strain level of 8.08%, as

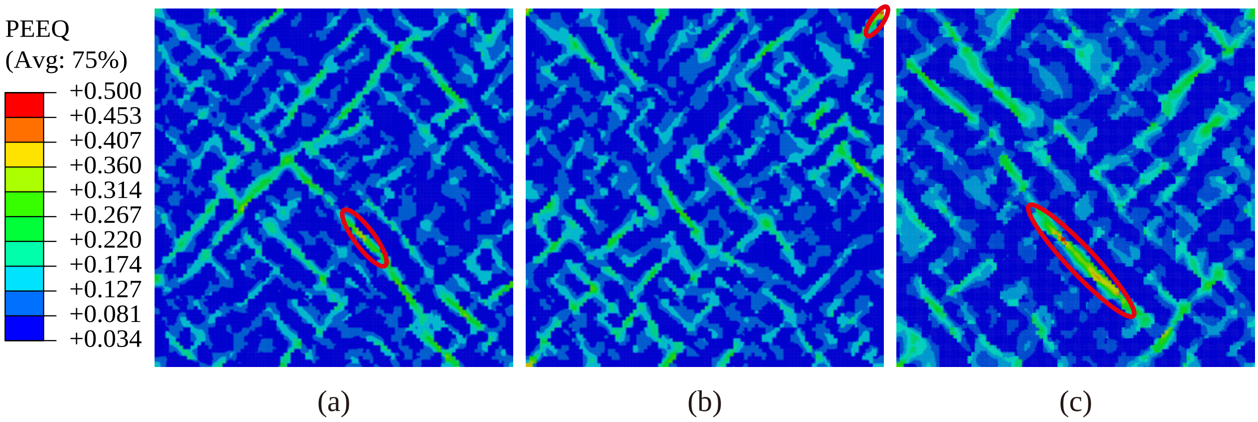

Figure 17: Influence of parameter C_M on the microscopic plasticity behavior: equivalent plastic strain distribution of RVEs generated with $P_M = 0.55$ and C_M equal to (a) 0.43, (b) 0.48 and (c) 0.55 at the macroscopic strain level of 8.08%. (The region with maximum values of plastic strain are located using red ellipses.)

shown in Fig. 17. The comparison clearly indicates that the localized microscopic strain rises with the increase of the parameter C_M. The highest maximum plastic strain value (red ellipses in Fig. 17) is found in the case with largest C_M among the tested four cases. It occurs mainly due to the presence of large martensite clusters within the RVE with $C_M = 0.55$ (Fig. 15c), and it affects the formation of shear bands which accommodate large strains along the martensite-ferrite interfaces.

5. Conclusions and prespectives

Plastic behavior of DP steels was investigated using topology optimization based artificial microstructures. Numerical simulations were performed using RVEs which contain artificial microstructures, with periodic boundary conditions, to study the influence of different loading scenarios and microstructural features on the overall and microscopic plastic behaviors.

Periodic boundary conditions corresponding to uniaxial tension, compression and shear tests, were deduced to deform the micromechanical models. During the deformation, shear bands were observed along the interface between different phases in each case. During the tensile and compressive tests, the path of shear bands is around 45° to the loading direction. Nevertheless, due to the presence of deformation induced twisting movement of martensite grains, which is caused by the shear loading, the direction of strain localization is 0° or 90° to the coordinate system. The effective plastic stress-strain response of each loading case, was also derived with the AEH scheme. Since relatively larger deformation occurs within ferrite phase, the stress-strain response during the shear loading is lower than that of the other two cases.

Moreover, two controlling parameters, which are used to generate various artificial RVEs, are adopted to investigate the influence of martensite phase fraction and distribution on the macroscopic and microscopic plastic behaviors. In the parametric analysis of two controlling parameters, it is found that, the increase of martensite fraction results to the strengthening of the effective flow properties and strain localization of DP steel. Since longer martensite-ferrite interface exists in artificial RVE with smaller C_M, it requires less energy to perform the same overall plastic strain. Therefore, the prediction from the artificial RVE with smaller C_M underestimates the effective flow properties. Conversely, the strain localization rises with the clustering of martensite phase, which corresponds to the decrease of the martensite-ferrite interface length, and controlled by assigning larger C_M for the RVE models.

Since the grain size effect has not been considered in the dislocation based theory of the present work, the grain size effect on the macroscopic and microscopic plastic behaviors was not discussed. To investigate the grain size effect, the micromechanical modeling should be extended with strain- or stress- gradient plasticity [42]. Strain-gradient plasticity takes into account the hardening caused by geometrically necessary dislocations (GNDs) in the computation of flow behavior. While, stress-gradient plasticity is based on the mechanism of dislocation pile-ups at the grain boundaries [43]. Both methods could be used to capture the grain size effect. Furthermore, the key difficulty during the extension of artificial microstructures in 3D case is that, the computation time dramatically rises as the dimension increases. Hence, further investigations are required to overcome these challenges.

Acknowledgements

Authors acknowledge Dr. Lv Zhao, Institute of Mechanics, Materials and Civil Engineering, UCLouvain, for fruitful discussions on the topic of triaxiality and damage evolution under various loading conditions. This work is funded by ESI Group, National Natural Science Foundation of China (NSFC, 11702254), China Postdoctoral Science Foundation (2018M642777), Henan Province Science and Technology Key Project (182102210186).

References

[1] N. Kim, G. Thomas, Effects of morphology on the mechanical behavior of a dual phase Fe/2Si/0.1 C steel, Metallurgical Transactions A 12 (3) (1981) 483–489.

[2] M. Sarwar, R. Priestner, Influence of ferrite-martensite microstructural morphology on tensile properties of dual-phase steel, Journal of Materials Science 31 (8) (1996) 2091–2095.

[3] A.-P. Pierman, O. Bouaziz, T. Pardoen, P. Jacques, L. Brassart, The influence of microstructure and composition on the plastic behaviour of dual-phase steels, Acta Materialia 73 (2014) 298–311.

[4] Y. Hou, T. Sapanathan, A. Dumon, P. Culière, M. Rachik, A novel artificial dual-phase microstructure generator based on topology optimization, Computational Materials Science 123 (2016) 188–200.

[5] Y. Hou, T. Sapanathan, A. Dumon, P. Culière, M. Rachik, A novel development of bi-level reduced surrogate model to predict ductile fracture behaviors, Engineering Fracture Mechanics 188 (2018) 232–249.

[6] G. Shen, B. Hu, C. Zheng, J. Gu, D. Li, Coupled simulation of ferrite recrystallization in a dual-phase steel considering deformation heterogeneity at mesoscale, Computational Materials Science 149 (2018) 191–201.

[7] E. Nesterova, S. Bouvier, B. Bacroix, Microstructure evolution and mechanical behavior of a high strength dual-phase steel under monotonic loading, Materials Characterization 100 (2015) 152–162.

[8] F. Al-Abbasi, Predicting the effect of ultrafine ferrite on the deformation behavior of DP-steels, Computational Materials Science 119 (2016) 90–107.

[9] Z. Xiong, A. A. Saleh, A. Kostryzhev, E. V. Pereloma, Strain-induced ferrite formation and its effect on mechanical properties of a dual phase steel produced using laboratory simulated strip casting, Journal of Alloys and Compounds 721 (2017) 291–306.

[10] X. Wei, S. Asgari, J. Wang, B. Rolfe, H. Zhu, P. Hodgson, Micromechanical modelling of bending under tension forming behaviour of dual phase steel 600, Computational Materials Science 108 (2015) 72–79.

[11] X. Sun, K. S. Choi, A. Soulami, W. N. Liu, M. A. Khaleel, On key factors influencing ductile fractures of dual phase (DP) steels, Materials Science and Engineering: A 526 (1-2) (2009) 140–149.

[12] V. Uthaisangsuk, U. Prahl, W. Bleck, Characterisation of formability behaviour of multiphase steels by micromechanical modelling, International Journal of Fracture 157 (1-2) (2009) 55.

[13] N. Vajragupta, V. Uthaisangsuk, B. Schmaling, S. Münstermann, A. Hartmaier, W. Bleck, A micromechanical damage simulation of dual phase steels using XFEM, Computational Materials Science 54 (2012) 271–279.

[14] T. Sirinakorn, S. Sodjit, V. Uthaisangsuk, Influences of microstructure characteristics on forming limit behavior of dual phase steels, steel research international 86 (12) (2015) 1594–1609.

[15] M. Nygårds, P. Gudmundson, Micromechanical modeling of ferritic/pearlitic steels, Materials Science and Engineering: A 325 (1) (2002) 435–443.

[16] M. Nygårds, P. Gudmundson, Three-dimensional periodic Voronoi grain models and micromechanical FE-simulations of a two-phase steel, Computational Materials Science 24 (4) (2002) 513–519.

[17] A. Fillafer, C. Krempaszky, E. Werner, On strain partitioning and micro-damage behavior of dual-phase steels, Materials Science and Engineering: A 614 (2014) 180–192.

[18] N. H. Abid, R. K. A. Al-Rub, A. N. Palazotto, Computational modeling of the effect of equiaxed heterogeneous microstructures on strength and ductility of dual phase steels, Computational Materials Science 103 (2015) 20–37.

[19] T. De Geus, R. Peerlings, M. Geers, Microstructural topology effects on the onset of ductile failure in multi-phase materials–A systematic computational approach, International Journal of Solids and Structures 67 (2015) 326–339.

[20] T. De Geus, M. Cottura, B. Appolaire, R. Peerlings, M. Geers, Fracture initiation in multi-phase materials: A systematic three-dimensional approach using a FFT-based solver, Mechanics of Materials 97 (2016) 199–211.

[21] T. de Geus, F. Maresca, R. Peerlings, M. Geers, Microscopic plasticity and damage in two-phase steels: On the competing role of crystallography and phase contrast, Mechanics of Materials 101 (2016) 147–159.

[22] J. Pagenkopf, A. Butz, M. Wenk, D. Helm, Virtual testing of dual-phase steels: Effect of martensite morphology on plastic flow behavior, Materials Science and Engineering: A 674 (2016) 672–686.

[23] R. Rodriguez, I. Gutierrez, Mechanical behaviour of steels with mixed microstructures, Proceeding of TMP 4 (2004) 356–363.

[24] J. H. Halton, Algorithm 247: Radical-inverse quasi-random point sequence, Communications of the ACM 7 (12) (1964) 701–702.

[25] L. Xia, P. Breitkopf, Design of materials using topology optimization and energy-based homogenization approach in Matlab, Structural and multidisciplinary optimization 52 (6) (2015) 1229–1241.

[26] L. Xia, D. Da, J. Yvonnet, Topology optimization for maximizing the fracture resistance of quasi-brittle composites, Computer Methods in Applied Mechanics and Engineering 332 (2018) 234 – 254.

[27] L. Xia, L. Zhang, Q. Xia, T. Shi, Stress-based topology optimization using bi-directional evolutionary structural optimization method, Computer Methods in Applied Mechanics and Engineering 333 (2018) 356 – 370.

[28] P. W. Chung, K. K. Tamma, R. R. Namburu, Asymptotic expansion homogenization for heterogeneous media: computational issues and applications, Composites Part A: Applied Science and Manufacturing 32 (9) (2001) 1291–1301.

[29] L. Meng, P. Breitkopf, G. Le Quilliec, An insight into the identifiability of material properties by instrumented indentation test using manifold approach based on ph curve and imprint shape, International Journal of Solids and Structures 106 (2017) 13–26.

[30] L. Meng, P. Breitkopf, B. Raghavan, G. Mauvoisin, O. Bartier, X. Hernot, On the study of mystical materials identified by indentation on power law and voce hardening solids, International Journal of Material Forming (2018) 1–16.

[31] M. Jafari, S. Ziaei-Rad, N. Saeidi, M. Jamshidian, Micromechanical analysis of martensite distribution on strain localization in dual phase steels by scanning electron microscopy and crystal plasticity simulation, Materials Science and Engineering: A 670 (2016) 57–67.

[32] S. R. Kalidindi, C. A. Bronkhorst, L. Anand, Crystallographic texture evolution in bulk deformation processing of FCC metals, Journal of the Mechanics and Physics of Solids 40 (3) (1992) 537–569.

[33] Q. Lai, L. Brassart, O. Bouaziz, M. Gouné, M. Verdier, G. Parry, A. Perlade, Y. Bréchet, T. Pardoen, Influ-

ence of martensite volume fraction and hardness on the plastic behavior of dual-phase steels: Experiments and micromechanical modeling, International Journal of Plasticity 80 (2016) 187–203.
[34] W. Bleck, Material Science of Steel: Textbook for RWTH Students, Mainz, 2007.
[35] A. Ramazani, K. Mukherjee, H. Quade, U. Prahl, W. Bleck, Correlation between 2D and 3D flow curve modelling of DP steels using a microstructure-based RVE approach, Materials Science and Engineering: A 560 (2013) 129–139.
[36] ABAQUS/Standard: User's Manual, Hibbitt, Karlsson & Sorensen, 1998.
[37] Z. Xia, C. Zhou, Q. Yong, X. Wang, On selection of repeated unit cell model and application of unified periodic boundary conditions in micro-mechanical analysis of composites, International Journal of Solids and Structures 43 (2) (2006) 266–278.
[38] W. Li, H. Gao, H. Nakashima, S. Hata, W. Tian, In-situ study of the deformation-induced rotation and transformation of retained austenite in a low-carbon steel treated by the quenching and partitioning process, Materials Science and Engineering: A 649 (2016) 417–425.
[39] M. Dunand, D. Mohr, On the predictive capabilities of the shear modified gurson and the modified mohrcoulomb fracture models over a wide range of stress triaxialities and lode angles, Journal of the Mechanics and Physics of Solids 59 (7) (2011) 1374–1394.
[40] T. de Geus, R. Peerlings, M. Geers, Microstructural modeling of ductile fracture initiation in multi-phase materials, Engineering Fracture Mechanics 147 (2015) 318–330.
[41] T. de Geus, R. Peerlings, M. Geers, Competing damage mechanisms in a two-phase microstructure: How microstructure and loading conditions determine the onset of fracture, International Journal of Solids and Structures 97 (2016) 687–698.
[42] H. Lyu, M. Hamid, A. Ruimi, H. M. Zbib, Stress/strain gradient plasticity model for size effects in heterogeneous nano-microstructures, International Journal of Plasticity 97 (2017) 46–63.
[43] D. Liu, Y. He, B. Zhang, L. Shen, A continuum theory of stress gradient plasticity based on the dislocation pile-up model, Acta Materialia 80 (2014) 350–364.